



ALMA CO Observations of Supernova Remnant N63A in the Large Magellanic Cloud: Discovery of Dense Molecular Clouds Embedded within Shock-ionized and Photoionized Nebulae

H. Sano^{1,2}, H. Matsumura³, T. Nagaya², Y. Yamane², R. Z. E. Alsaberi⁴, M. D. Filipovic⁴, K. Tachihara², K. Fujii⁵, K. Tokuda^{6,7}, K. Tsuge², S. Yoshiike², T. Onishi⁶, A. Kawamura⁷, T. Minamidani^{8,9}, N. Mizuno⁸, H. Yamamoto², S. Inutsuka², T. Inoue², N. Maxted¹⁰, G. Rowell¹¹, M. Sasaki¹², and Y. Fukui^{1,2}

¹ Institute for Advanced Research, Nagoya University, Furo-cho, Chikusa-ku, Nagoya 464-8601, Japan; sano@phys.nagoya-u.ac.jp

² Department of Physics, Nagoya University, Furo-cho, Chikusa-ku, Nagoya 464-8601, Japan; nagaya@phys.nagoya-u.ac.jp, yamane@phys.nagoya-u.ac.jp

³ Kavli Institute for the Physics and Mathematics of the Universe (WPI), The University of Tokyo Institutes for Advanced Study, The University of Tokyo, 5-1-5 Kashiwanoha, Kashiwa, Chiba 277-8583, Japan; hideaki.matsumura@ipmu.jp

⁴ Western Sydney University, Locked Bag 1797, Penrith South DC, NSW 1797, Australia; R.Alsaberi@westernsydney.edu.au, M.Filipovic@westernsydney.edu.au

⁵ Department of Astronomy, School of Science, The University of Tokyo, 7-3-1 Hongo, Bunkyo-ku, Tokyo 133-0033, Japan

⁶ Department of Physical Science, Graduate School of Science, Osaka Prefecture University, 1-1 Gakuen-cho, Naka-ku, Sakai 599-8531, Japan

⁷ National Astronomical Observatory of Japan, Mitaka, Tokyo 181-8588, Japan

⁸ Nobeyama Radio Observatory, National Astronomical Observatory of Japan (NAOJ), National Institutes of Natural Sciences (NINS), 462-2, Nobeyama,

Minamimaki, Minamisaku, Nagano 384-1305, Japan

⁹ Department of Astronomical Science, School of Physical Science, SOKENDAI (The Graduate University for Advanced Studies), 2-21-1, Osawa, Mitaka, Tokyo 181-8588, Japan

¹⁰ School of Sciences, University of New South Wales, Australian Defence Force Academy, Canberra, ACT 2600, Australia

¹¹ School of Physical Sciences, The University of Adelaide, North Terrace, Adelaide, SA 5005, Australia

¹² Dr. Karl Remeis-Sternwarte, Erlangen Centre for Astroparticle Physics, Friedrich-Alexander-Universität Erlangen-Nürnberg, Sternwartstraße 7, D-96049 Bamberg, Germany

Received 2018 September 7; revised 2019 January 28; accepted 2019 January 28; published 2019 March 1

Abstract

We carried out new $^{12}\text{CO}(J=1-0, 3-2)$ observations of a N63A supernova remnant (SNR) from the LMC using the Atacama Large Millimeter/submillimeter Array (ALMA) and Atacama Submillimeter Telescope Experiment. We find three giant molecular clouds toward the northeast, east, and near the center of the SNR. Using the ALMA data, we spatially resolved clumpy molecular clouds embedded within the optical nebulae in both the shock-ionized and photoionized lobes discovered by previous $\text{H}\alpha$ and $[\text{S II}]$ observations. The total mass of the molecular clouds is $\sim 800 M_{\odot}$ for the shock-ionized region and $\sim 1700 M_{\odot}$ for the photoionized region. Spatially resolved X-ray spectroscopy reveals that the absorbing column densities toward the molecular clouds are $\sim (1.5-6.0) \times 10^{21} \text{ cm}^{-2}$, which are $\sim 1.5-15$ times less than the averaged interstellar proton column densities for each region. This means that the X-rays are produced not only behind the molecular clouds, but also in front of them. We conclude that the dense molecular clouds have been completely engulfed by the shock waves, but have still survived erosion owing to their high density and short interacting time. The X-ray spectrum toward the gas clumps is well explained by an absorbed power-law model or a high-temperature plasma model, in addition to thermal plasma components, implying that the shock-cloud interaction is efficiently working for both cases through the shock ionization and magnetic field amplification. If the hadronic gamma-ray is dominant in the GeV band, the total energy of the cosmic-ray protons is calculated to be $\sim (0.3-1.4) \times 10^{49} \text{ erg}$, with an estimated interstellar proton density of $\sim 190 \pm 90 \text{ cm}^{-3}$, containing both the shock-ionized gas and neutral atomic hydrogen.

Key words: cosmic rays – ISM: clouds – ISM: individual objects (LHA 120-N 63A) – ISM: supernova remnants – photon-dominated region (PDR)

1. Introduction

It is a longstanding question how neutral interstellar gas is ionized. Massive stars and supernova remnants (SNRs) are thought to be the primary sources of gas ionization in galaxies. Their natal gas is rapidly disrupted by powerful UV radiation into the photoionized gas on timescales of ~ 10 Myr after the formation of massive star clusters (e.g., Fukui et al. 1999; Kawamura et al. 2009). Dense neutral gas within a low-density wind-blown bubble will be evaporated by supernova shocks, if the interacting time is longer than $\sim 10^5$ yr (e.g., McKee & Ostriker 1977; Celli et al. 2018). Owing to their short timescales, it is difficult to examine an evolutionary process from the neutral gas to the ionized gas observationally.

SNR N63A (also known as MCSNR 0535–6602, LHA 120-N63A, or SNR B0535–66.0) provides an ideal laboratory for studying the evolution of interstellar gas and shock-cloud interactions. N63A is one of the brightest SNRs in the Large Magellanic Cloud (LMC), whose size is $81'' \times 67''$ or ~ 18 pc in diameter, assuming a distance of 50 kpc (e.g., Dickel et al. 1993; Warren et al. 2003; Bozzetto et al. 2017). The age of the SNR is estimated to be 2000–5000 yr (Hughes et al. 1998; Warren et al. 2003), indicating that the natal gas may still be associated with N63A. The SNR appears to be embedded within the H II region N63 coincident with the OB association NGC 2030 or LH83 (Chu & Kennicutt 1988; Lucke & Hodge 1970). N63A is therefore believed to be the remnant of a massive star in the association (e.g., van den Bergh & Dufour 1980; Shull 1983; Hughes et al. 1998).

The core-collapse origin was also confirmed by detailed measurements of Fe $K\alpha$ centroids (Yamaguchi et al. 2014).

The SNR holds an optical nebula (diameter is ~ 6 pc) within the shell, which comprises three prominent lobes (Mathewson et al. 1983). The two eastern lobes with high-intensity ratios of $[S\ II]/H\alpha$ (0.7; Payne et al. 2008) represent the shock-ionized gas, while the other western lobe with a low-intensity ratio corresponds to the photoionized gas (Levenson et al. 1995). Furthermore, all optical lobes show molecular shock properties with their near-infrared colors, suggesting that the shocked molecular gas dominates in the SNR (Williams et al. 2006). Subsequent detailed infrared spectroscopy confirmed that shock-excited molecular hydrogen lines are detected in all optical lobes (Caulet & Williams 2012). The imaging spectroscopy of X-rays also indicates the presence of dense interstellar gas with a mass of at least $\sim 450 M_{\odot}$ (Warren et al. 2003).

The CO clouds associated with the optical nebula have not yet been detected despite a number of attempts (e.g., Cohen et al. 1988; Israel et al. 1993; Desai et al. 2010). CO observations with the NANTEN2 4 m telescope and the Mopra 22 m telescope have detected a giant molecular cloud (GMC) only in the northeastern edge of the shell, whereas no significant CO emission lines have been detected toward the optical nebula (Yamaguchi et al. 2001; Sano et al. 2017a).

In the present paper, we show the first detection of dense molecular clouds associated with the optical nebula in N63A using the $^{12}\text{CO}(J = 1-0, 3-2)$ emission lines with the Atacama Large Millimeter/submillimeter Array (ALMA) and the Atacama Submillimeter Telescope Experiment (ASTE). Morphological matching of molecular clouds with the optical, X-ray, or radio continuum nebula reveals new information on the origin of the ionized gas in SNR N63A. Section 2 describes observations and data reductions of CO, radio continuum, and X-rays. Section 3.1 gives large-scale views of CO, HI, and X-rays; Section 3.1 presents a detailed CO distribution with ALMA; Sections 3.3 and 3.4 present a X-ray spectral analysis and comparisons of the X-ray absorbing column density with the interstellar medium (ISM). A discussion and conclusions are provided in Sections 4 and 5, respectively. In a subsequent paper, we will present a detailed analysis of the X-ray spectra for the whole SNR and compare the spectra with CO maps and other available data sets.

2. Observations and Data Reductions

2.1. CO

Observations of the $^{12}\text{CO}(J = 3-2)$ emission line were carried out in 2015 November 16–24 using ASTE (Ezawa et al. 2004), which is operated by the National Astronomical Observatory of Japan (NAOJ). We observed a $3' \times 3'$ rectangular region centered at $(\alpha_{J2000}, \delta_{J2000}) \sim (05^{\text{h}}35^{\text{m}}43^{\text{s}}.7, -66^{\circ}02'11''.8)$ using the on-the-fly mapping mode with Nyquist sampling. The front end was the “DASH 345” receiver. The digital FX spectrometer “MAC” (Sorai et al. 2000) was used for the back end, whose bandwidth is 128 MHz with 1024 channels, corresponding to a velocity coverage of ~ 111 km s^{-1} and a resolution of ~ 0.11 km s^{-1} . The typical system temperature is ~ 300 – 400 K in the single-side band, including the atmosphere. We observed N159W $[(\alpha_{J2000}, \delta_{J2000}) \sim (05^{\text{h}}40^{\text{m}}3^{\text{s}}.7, -68^{\circ}47'00'')]$ (Minamidani et al. 2011), and then we estimated the main beam efficiency of ~ 0.52 . We also checked the pointing accuracy every half-hour to satisfy an offset

within $2''$. After applying two-dimensional Gaussian smoothing, the final beam size is to be $\sim 25''$. The noise fluctuation is ~ 0.18 K at a velocity resolution of ~ 0.4 km s^{-1} .

Observations of the $^{12}\text{CO}(J = 1-0)$ emission line were carried out in 2016 January 31 and August 27 using ALMA Band 3 (86–116 GHz) as a Cycle 3 project #2015.1.01130.S. We utilized the mosaic mapping mode of a $100'' \times 100''$ rectangular region centered at $(\alpha_{J2000}, \delta_{J2000}) \sim (05^{\text{h}}35^{\text{m}}46^{\text{s}}.37, -66^{\circ}02'04''.8)$. The observations were conducted using 38 antennas of the 12 m array. The baseline length ranges from 13.7 to 1551.1 m, corresponding to $u-v$ distances from 4.6 to 596.0 $k\lambda$. The correlator was set up in dual polarization mode with a bandwidth of 58.59 MHz, corresponding to a velocity coverage of 152.5 km s^{-1} . Three quasars, J0635–7516, J0519–4546, and J0529–7245, were observed as the complex gain calibrator, the flux calibrator, and the phase calibrator, respectively. The data reduction, including the calibration, was performed using the Common Astronomy Software Application (CASA; McMullin et al. 2007) package version 5.1.0. We utilized the multiscale CLEAN algorithm implemented in the CASA package (Cornwell 2008). The beam size of the final data sets is $1''.93 \times 1''.71$ with a position angle of $66^{\circ}.6$, corresponding to a spatial resolution of ~ 0.4 pc at an LMC distance of ~ 50 kpc (e.g., Maggi et al. 2016; Bozzetto et al. 2017). The typical noise fluctuation is ~ 0.84 K at a velocity resolution of 0.4 km s^{-1} . To estimate the missing flux, we used the $^{12}\text{CO}(J = 1-0)$ data sets obtained with Mopra (Sano et al. 2017a). Northeast of the SNR, we compared the integrated intensities of Mopra and ALMA CO data that are smoothed to match the FWHM resolution of $\sim 45''$. We obtained a missing flux of $\sim 10\%$ or less, hence the missing flux is considered to be negligible.

2.2. X-Rays

We use archived X-ray data obtained with the *Chandra X-ray Observatory*, for which the observation ID is 777 (PI: Hughes Warren et al. 2003). The data were taken with the Advanced CCD Imaging Spectrometer S-array (ACIS-S3) on 2000 October 16–17. We used the *Chandra* Interactive Analysis of Observations (CIAO; Fruscione et al. 2006) software version 4.10 with CALDB 4.7.8 for data reduction, imaging, and spectroscopic analysis. The data were reprocessed using the *chandra_repro* procedure. We created energy-filtered, exposure-corrected images using the *fluximage* procedure in the energy bands of 0.3–0.6 keV, 0.6–1.1 keV, 1.1–6.0 keV, 4.3–6.0 keV, and 0.3–6.0 keV. The total effective exposure time is 43.4 ks. For the spectral analysis, we used HEASOFT (version 6.24), including spectral fitting with XSPEC (version 12.10.0c). We fit the spectrum in the energy band from 0.4–6.0 keV and the errors of model fit are quoted at 90% confidence levels. We also used the ATOMDB version 3.0.9.

2.3. Radio Continuum

We make use of archival Australia Telescope Compact Array (ATCA) data obtained from the Australia Telescope Online Archive. We analyzed data from projects C058, CX310, and C3229 that were taken in 1991, 1992, 1997, 2015, and 2018. These observations include pre-Compact Array Broadband Backend (pre-CABB) and CABB in various array configuration such as 6A, 1.5B, 1.5C, 6C, 375, and EW352 (for details see Table 1). The primary (flux density) calibration was done using source PKS 1934–638, while the secondary (phase) calibrators were PKS 0454–810 (in 1991), PKS 0407–658 (in 1992), and

Table 1
ATCA Observations of N63A Used in This Study

Observing Date	Frequency (MHz)	Array Configuration	Total Obs. Time (minutes)	Bandwidth (MHz)	Channels	References and Notes
pre CABB						
1991 May 2	4786	6A	15.7	128	33	Dickel et al. (1993)
1991 May 3	4786	6A	...	128	33	Dickel et al. (1993)
1991 May 22	5746	1.5B	...	128	33	Dickel et al. (1993)
1991 May 23	5746–8640	1.5B	1.3	128	33	Dickel et al. (1993)
1991 May 24	8640	1.5B	...	128	33	Dickel et al. (1993)
1992 Aug 17	4786–8640	1.5C	668	128	33	Dickel et al. (1993)
1992 Oct 20	4786–8640	6C	573	128	33	Dickel et al. (1993)
1997 Apr 6	4786–8640	375	40	128	33	Bozzetto et al. (2017)
CABB						
2015 Jan 1	5500–9000	6A	42	2048	2049	This work
2015 Jan 2	2100	6A	150	2048	2049	This work
2018 Mar 27	5500–9000	EW352	34	2048	2049	This work

PKS 0530–727 (in 2015 and 2018). Data reduction and imaging were accomplished using the MIRIAD¹³ (Sault et al. 1995) and KARMA¹⁴ (Gooch 1997) software packages. The images were formed using MIRIAD multi-frequency synthesis (Sault & Wieringa 1994) and Briggs weighting of $robust = 0$ and 1. They were deconvolved with primary beam correction applied. The same procedure was used for both Q and U Stokes parameters.

The pre-CABB images at 4786 and 8640 MHz have a resolution of $2''.9 \times 2''.0$ and $3''.5 \times 2''.7$. However, our CABB images at all frequencies suffer from the insufficient $u-v$ coverage but we still manage to achieve reasonable sensitivity and resolutions of $5''.7 \times 4''.9$ at 2100 MHz, $2''.7 \times 1''.5$ at 5500 MHz, and $1''.2 \times 0''.8$ at 9000 MHz (Table 2). While our pre-CABB images are of better sensitivity than newer but incomplete $u-v$ coverage CBB images, the new CABB polarization images can show good polarization regions.¹⁵

2.4. Astronomical Data at the Other Wavelengths

Optical data ($H\alpha$, [S II], and [O III]) are used to derive the spatial distribution and density of the ionized gas. We utilized the *Hubble Space Telescope* (HST) WFPC2 images of N63A, which are downloaded from the Hubble Legacy Archive. The observations were carried out using the F656N ($H\alpha$), F673N ([S II]), and F502N ([O III]) filters on 1997 October 8 and 2000 September 12. The exposure times of $H\alpha$, [S II], and [O III] are ~ 1000 s, ~ 1200 s, and ~ 2400 s, respectively. For further details about the data reductions, see the *HST* Data Handbooks.¹⁶

We also use the archived H I data obtained with the ATCA & the Parkes Radio Telescope (Kim et al. 2003). The combined H I image has an angular resolution of $\sim 1'$, corresponding to a spatial resolution of ~ 15 pc. Typical noise fluctuations are ~ 0.3 K at a velocity resolution of 1.56 km s^{-1} .

¹³ <http://www.atnf.csiro.au/computing/software/miriad/>

¹⁴ <http://www.atnf.csiro.au/computing/software/karma/>

¹⁵ Note that ATCA polarization capacity came online only in mid-1993, i.e., before the images presented here at 4786 and 8640 MHz.

¹⁶ http://www.stsci.edu/hst/HST_overview/documents/datahandbook/

Table 2
Details of the ATCA Radio Continuum Images of N63A

Frequency (MHz)	Beam Size (arcsec)	rms (σ) (mJy beam ⁻¹)	PA (degree)
2100	$5''.7 \times 4''.9$	0.10	0.4
4786	$2''.9 \times 2''.0$	0.31	80.4
5500	$2''.7 \times 1''.5$	0.25	11.2
8640	$3''.5 \times 2''.7$	0.89	78.8
9000	$1''.2 \times 0''.8$	0.11	11.4

3. Results

3.1. Large-scale Views of X-Rays, Radio Continuum, CO, and H I

Figures 1(a) and (b) show the three-color images of X-rays and radio continuum, respectively. The X-ray shell shows an elliptical shape, slightly elongated in the northeastern direction, with a diffuse blow-out structure in the southwest. The X-ray hole inside the SNR, also mentioned by Warren et al. (2003), spatially coincides with the optical nebula at $(\alpha_{J2000}, \delta_{J2000}) \sim (05^{\text{h}}35^{\text{m}}43.^{\text{s}}1, -66^{\circ}01'59'')$. The radio continuum emission peaks at the same central place where the optical emission is detected and coincides with the featured X-ray hole. The north, east, and southeast areas of N63A closely follow the X-ray emission. We also find a clear indication of a steepening of the radio spectral index (reddish color) at the southeast limb, as well as in the north, suggesting that the synchrotron radio emission dominates in these regions. However, toward the southwest side of the SNR we did not detect any radio emission, which is probably due to the insufficient sensitivity of our radio images (Figure 1(b)). A linear polarization image of N63A at 5500 MHz was created using the Q and U Stokes parameters and is shown in Figure 1(c). However, no reliable polarization images could be created at 9000 MHz, due to the low signal-to-noise ratio caused by poor uv coverage. The fractional polarization has been evaluated using the standard MIRIAD task IMPOL. Our estimated peak fractional polarization value is $P = 5\% \pm 1\%$, while the average polarization is about $\sim 3\%$. This is unusually weak for a young SNR and very similar to the earlier Dickel et al. (1993) results, especially when compared to the range of

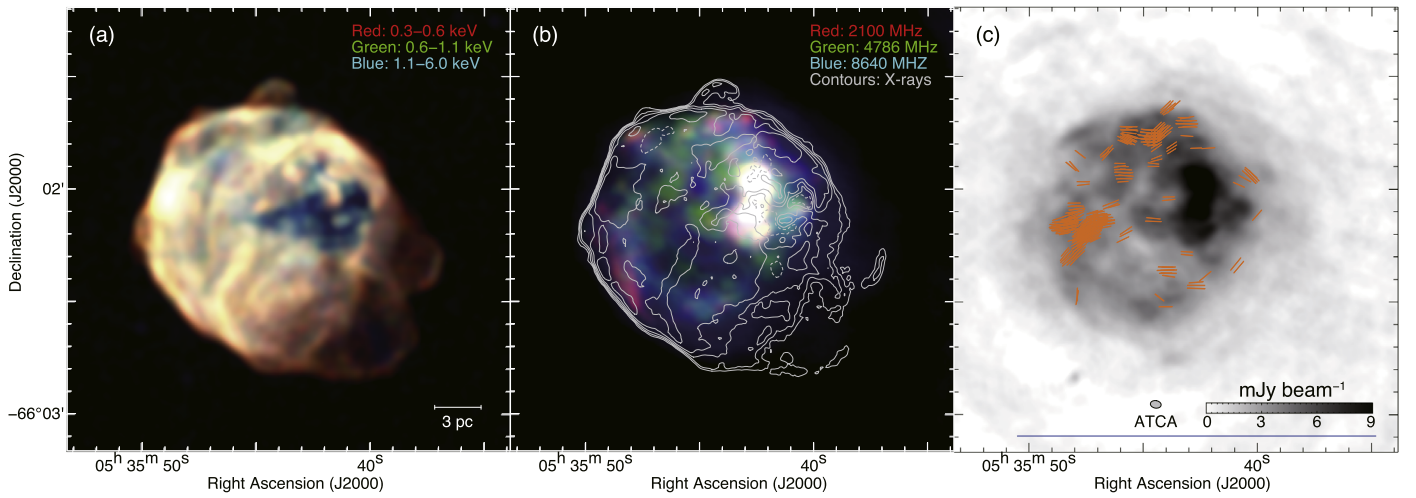


Figure 1. Three-color image of N63A obtained with (a) *Chandra* X-rays red: 0.3–6.0 keV; green: 0.6–1.1 keV; and blue: 1.1–6.0 keV and (b) ATCA (red: 2100 MHz; green: 4786 MHz; and blue: 8640 MHz). The superposed contours indicate the broadband X-rays in the energy band from 0.3–6.0 keV, whose contour levels are 0.4, 0.8, 1.6, 3.2, 6.4, and 12.8×10^{-6} counts $\text{s}^{-1} \text{pixel}^{-1}$. (c) Fractional polarization vectors at 5500 MHz overlaid on a 4786 MHz ATCA (pre-CABB) image of N63A. The blue line represents a polarization vector of 100%. We used a $\text{robust}=0$ weighting scheme to make this image. The peak fractional polarization value is $P = 5\% \pm 1\%$, while the average polarization is measured to be $\sim 3\%$.

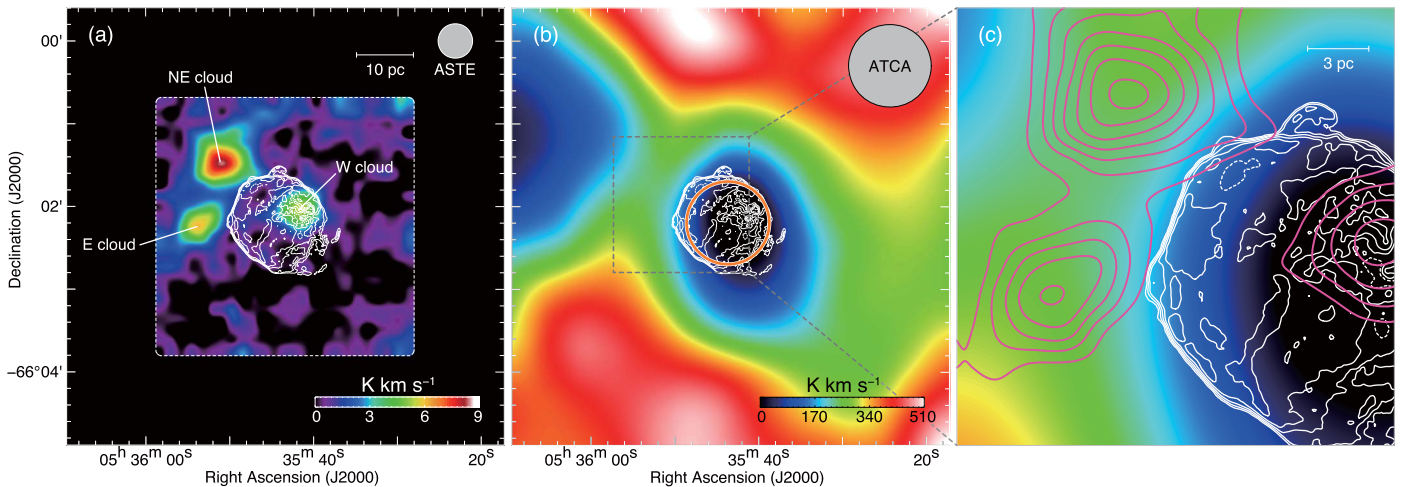


Figure 2. Integrated intensity maps of (a) ASTE $^{12}\text{CO}(J=3-2)$ and (b) ATCA & Parkes HI (Kim et al. 2003) toward N63A. The integration velocity range is $V_{\text{LSR}} = 276.8\text{--}288.0$ km s^{-1} . The superposed white contours indicate that the *Chandra* X-rays in the energy band of 0.3–6.0 keV are the same as those in Figure 1(b). (c) Enlarged view of the northeastern shell of the SNR inside the dashed box in Figure 2(b). The superposed magenta contours represent the $^{12}\text{CO}(J=3-2)$ integrated intensity. The lowest contour and contour intervals are 2 K km s^{-1} and 1 K km s^{-1} , respectively. We also show the beam size of ASTE CO and ATCA & Parkes HI, and the scale bar in the top right corners.

other LMC SNRs that we observed over the past decades with ATCA (Bojičić et al. 2007; Crawford et al. 2008a, 2008b, 2010; Cajko et al. 2009; Bozzetto et al. 2010, 2012a, 2012b, 2012c, 2012d, 2013, 2014a, 2014b; Haberl et al. 2012; Brantseg et al. 2014; Bozzetto & Filipović 2014; Kavanagh et al. 2015). Perhaps significant depolarization within the 2 GHz bandwidth is present.

Figure 2 shows the large-scale distributions of $^{12}\text{CO}(J=3-2)$ and HI toward SNR N63A. We find three GMCs whose sizes are $\sim 7\text{--}10$ pc. Two of them extend toward the northeast and east of the X-ray shell (hereafter referred to as the “NE cloud” and the “E cloud”), which correspond to the GMCs previously mentioned by Sano et al. (2017a). The other one lies just west of the center of the SNR. The GMC, hereafter referred to as the “W cloud,” spatially coincides not only with the X-ray hole, but also with the radio continuum peak or optical nebula. In the HI map, we find two cavity-like structures toward the

northeast and center of the SNR. The former corresponds to the HI shell GS 76 cataloged by Kim et al. (1999). The latter represents an HI absorption dip owing to the strong radio continuum emission from the optical nebula and SNR, which is similar to the case of LMC SNR N49 (Yamane et al. 2018) or N103B (Sano et al. 2018a). An enlarged view of the northeastern shell is shown in Figure 2(c). The northeastern X-ray shell appears to be associated not only with the NE and E clouds, but also with the HI wall.

Figure 3 shows the averaged CO and HI spectra toward SNR N63A. We find significant differences in the HI spectra toward the SNR (blue, inside the SNR) and its surroundings (cyan, outside the SNR). The negative HI brightness temperature at the velocity of ~ 278 km s^{-1} is the absorption line, which also suggests that there is HI located in front of the SNR. The CO spectrum has an intensity peak at $V_{\text{LSR}} \sim 281$ km s^{-1} , which is slightly shifted from the central velocity of the HI absorption line.

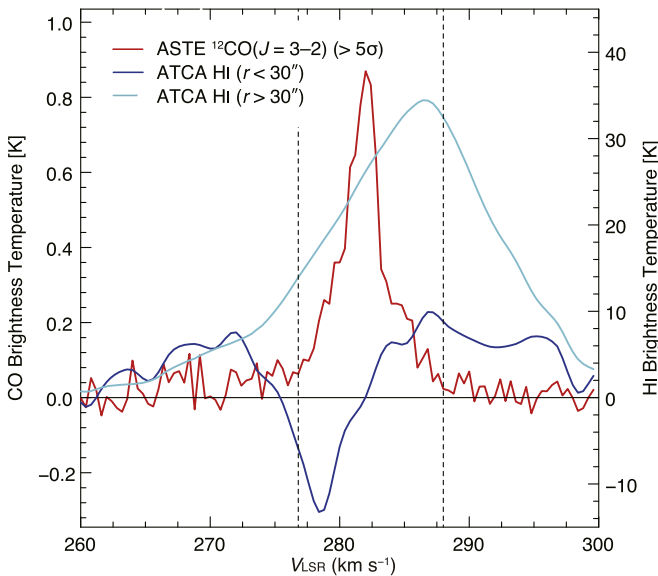


Figure 3. Averaged line profiles of $^{12}\text{CO}(J=3-2)$ (red) and HI (blue and cyan) toward SNR N63A. The blue and cyan profiles are spatially averaged HI spectra inside and outside of a circle with a radius of $30''$, as shown in Figure 2(b) (orange circle). The CO spectrum in red is averaged over the region where the integrated intensity is 2 K km s^{-1} or higher ($>5\sigma$). The velocity integration range used for the images in Figure 2 is also shown by dashed lines.

3.2. Detailed CO Distribution with ALMA

Figure 4 shows a three-color image of N63A composed of a combination of *HST* $\text{H}\alpha$ (red, Chu 2001), ALMA $^{12}\text{CO}(J=1-0)$ (green), and *Chandra* X-rays in the energy band of 0.3–6.0 keV (blue, Warren et al. 2003). We detect all the GMCs that we identified using the ASTE CO data. Since the E cloud is spatially separated from the X-ray shell, the GMC is probably not associated with the SNR. On the other hand, the NE cloud is elongated to the southwest direction, whose tip with a position at $(\alpha_{\text{J2000}}, \delta_{\text{J2000}}) \sim (05^{\text{h}}35^{\text{m}}47^{\text{s}}.8, -66^{\circ}01'38'')$ is adjacent to the northeastern X-ray shell. We also spatially resolved the W cloud into several CO clouds. The molecular clouds show clumpy distributions, which are likely embedded within the optical nebula and the X-ray shell.

To estimate the masses of GMCs, we utilize the following equations:

$$M = m_{\text{H}} \mu \Omega D^2 \sum_i [N_i(\text{H}_2)], \quad (1)$$

$$N(\text{H}_2) = X \cdot W(^{12}\text{CO}), \quad (2)$$

where m_{H} is the mass of atomic hydrogen, $\mu = 2.72$ is the mean molecular weight relative to atomic hydrogen, Ω is the solid angle of each pixel, D is the distance to the LMC, $N_i(\text{H}_2)$ is the molecular hydrogen column density for each pixel i , X is the CO-to- H_2 conversion factor, and $W(^{12}\text{CO})$ is the integrated intensity of the $^{12}\text{CO}(J=1-0)$. We used the conversion factor $X = 7.0 \times 10^{20} \text{ cm}^{-2} (\text{K km s}^{-1})^{-1}$ (Fukui et al. 2008). The physical properties of GMCs are estimated for the regions that are significantly detected by CO at $\sim 5\sigma$ or higher. We finally obtain the masses of the GMCs as $\sim 6400 M_{\odot}$ for the NE cloud, $\sim 3600 M_{\odot}$ for the E cloud, and $\sim 2600 M_{\odot}$ for the W cloud.

Figure 5 shows an enlarged view of the optical nebula obtained by *HST* [S II] (red), $\text{H}\alpha$ (green), and [O III] (blue). The northeast and southeast lobes, comprising the shock-ionized gas, show a crescent shape with many filamentary structures. In

contrast, the western lobe is smoothly distributed in $\text{H}\alpha$ with optical dark lanes and a compact H II region. We identified 11 molecular clouds, A–K, toward the optical nebula, as shown in the white contours. The definitions and basic physical properties of each cloud are listed in Table 3. The densest molecular clouds, named A, B, and D, show a good spatial correspondence with the optical dark lane, suggesting that these molecular clouds are located in front of the photoionized lobe. The peak proton column density of cloud B is $\sim 1 \times 10^{23} \text{ cm}^{-2}$, corresponding to $A_{\text{V}} \sim 40 \text{ mag}$ (e.g., Jenkins & Savage 1974). However, there is no clear evidence of an optical dark lane toward the molecular clouds G–K, which are associated with the shock-ionized lobes. This implies that these molecular clouds are located inside or behind the shock-ionized lobes. We also note that bright optical filaments, as shown in Figure 5, are in spatial alignment (in projection) with the molecular cloud H, possibly suggesting the shape of the filamentary structure is reflected by that of the natal molecular cloud before the shock ionization. The total mass of molecular clouds is $\sim 1700 M_{\odot}$ for the photoionized region (A–F) and $\sim 800 M_{\odot}$ for the shock-ionized region (G–K).

We find that the molecular cloud is also depressed toward the exciting star HD 271389 with a position at $(\alpha_{\text{J2000}}, \delta_{\text{J2000}}) \sim (05^{\text{h}}35^{\text{m}}40^{\text{s}}.68, -66^{\circ}02'05''.9)$. Based on photometry of $U - B = -0.853 \pm 0.082 \text{ mag}$ (Oey 1996) and $M_{\text{V}} = -3.6 \pm 0.5 \text{ mag}$ (Laval et al. 1986), B0V–B1V is reasonable for the spectral type of the exciting star (see also Pecaut & Mamajek 2013). The UV radiation and stellar winds therefore must be powerful enough to ionize the molecular cloud. In fact, several pillar-like structures surrounding the exciting star are seen; these have previously been mentioned by Caulet & Williams (2012). Further ALMA observations with fine angular resolutions of subarcseconds will allow us to study the photon-dominated region in detail.

Figure 6 shows a comparison among the X-rays (red: 0.3–0.6 keV; green: 0.6–1.1 keV; and blue: 1.1–6.0 keV), $\text{H}\alpha$, [S II], [O III], CO, and radio continuum with a center frequency of 4786 MHz (Dickel et al. 1993). The X-ray hole near the location of the optical nebula is considered to be the result of interstellar absorption by the dense gas cloud (Warren et al. 2003). We confirm that a particularly dark region in the X-ray hole shows a good spatial correspondence with the dense molecular clouds. Both the $\text{H}\alpha$ and [S II] emission also spatially coincide with the X-ray hole. Additionally, we find that the bright radio continuum emission shows a good spatial correspondence not only with the X-ray hole, but also with the $\text{H}\alpha$ nebula, suggesting that the radio continuum at $\sim 5 \text{ GHz}$ is dominated by the free-free radiation. The spatial extent of the molecular clouds, optical nebula, and/or radio continuum therefore spatially accounts for $\sim 80\%$ of the area of the X-ray hole. The remaining $\sim 20\%$ is placed to the south of the molecular clouds G, F, and J. These regions are possibly associated with dense HI clumps or diffuse ionized gas. In fact, if we take into account regions with a low radio continuum emission of $\sim 10 \text{ K}$, the X-ray hole is completely filled by the neutral gas and/or ionized gas.

We also note that X-rays are clearly enhanced around the northern shock-ionized lobe (see Figure 6(a)), and the edges of molecular clouds (see Figure 6(d)). The former regions are also bright in [O III] emission (Figure 6(c)), suggesting that the shock ionization occurred. The shock velocities of the [O III] bright regions are thought to be $\sim 120 \text{ km s}^{-1}$ and below

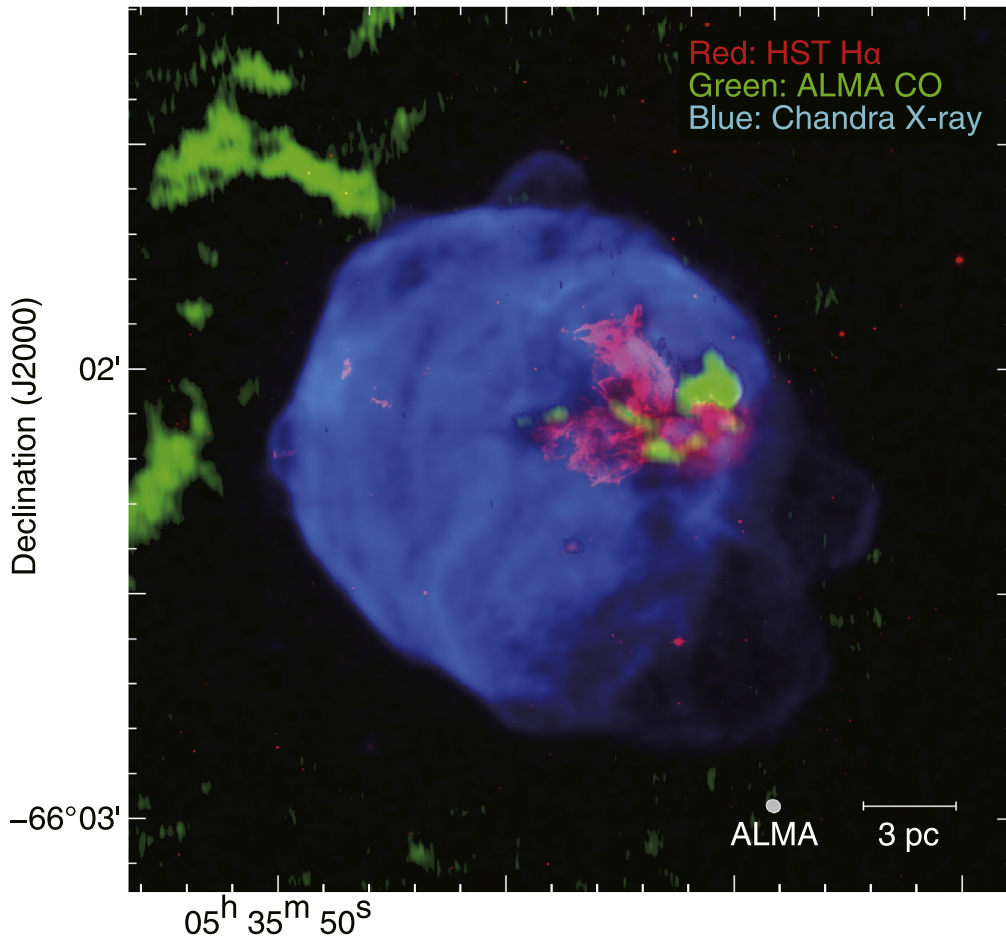


Figure 4. Three-color image of SNR N63A. The red, green, and blue colors represent the *HST* H α (Chu 2001), ALMA $^{12}\text{CO}(J = 1-0)$, and *Chandra* X-rays (E : 0.3–6.0 keV, Warren et al. 2003), respectively. The velocity range of CO is from 276.8 to 288.0 km s $^{-1}$. We also show the beam size of the ALMA CO observation and scale bar in the bottom right corner.

200 km s $^{-1}$ (e.g., Cox & Raymond 1985; Allen et al. 2008). However, the quoted shock velocities may be too slow to produce X-rays in these regions. It possibly means that shock waves are suddenly decelerated toward the region owing to the shock interaction with dense materials.

We estimate the number density of ionized protons n_p using the radio continuum data and following equation:

$$\tau_c(\nu) = 8.213 \times 10^{-2} T_e^{-1.35} (\nu/1 \text{ GHz})^{-2.1} \text{EM}, \quad (3)$$

$$T_b = T_e [1 - \exp(-\tau_c(\nu))], \quad (4)$$

where $\tau_c(\nu)$ is the optical depth of ionized gas, T_e is the electron temperature, T_b is the brightness temperature of the radio continuum emission, and EM is the emission measure. EM is defined as

$$\text{EM} = \int_0^{L_1} n_e n_p dl \sim n_p^2 L_1, \quad (5)$$

where n_e is the number density of ionized electrons and L_1 is the thickness of the ionized gas in units of parsecs. The mean brightness temperature is $\sim 43 \pm 7$ K for the shock-ionized region and $\sim 34 \pm 1$ K for the photoionized region. We obtain the ionized proton density $\sim 280 \pm 110$ cm $^{-3}$ for the shock-ionized region and $\sim 560 \pm 100$ cm $^{-3}$ for the photoionized region, assuming $L_1 \sim 5$ pc and $T_e = 14743$ K for the shock-ionized lobe and $L_1 \sim 1$ pc and $T_e = 14620$ K for the

photoionized lobes (Caulet & Williams 2012). These values are roughly consistent with estimates of ~ 250 cm $^{-3}$ from X-ray spectroscopy (Warren et al. 2003) and of ~ 50 –300 cm $^{-3}$ from optical studies (Shull 1983 and the references therein).

3.3. X-Ray Spectral Analysis

To compare the absorbing column density of X-rays with the interstellar gas density, we extract X-ray spectra from three regions as shown in Figure 6(d): the west (W), southeast (SE), and northeast (NE) regions. The W region covers the densest molecular clouds A, B, and D. The SE region represents the X-ray hole with clumpy molecular clouds, and NE corresponds to a reference region without dense clouds or ionized gas.

Figure 7 shows the background-subtracted ACIS-S spectra for each region. The background is selected as a source-free region with a central position of $(\alpha_{J2000}, \delta_{J2000}) \sim (05^{\text{h}}35^{\text{m}}31^{\text{s}}.6, -66^{\circ}03'30'')$, whose position is outside the SNR. Following the previous X-ray study in N63A (Warren et al. 2003), we first fitted the NE spectrum with a non-equilibrium ionization (NEI) plasma model using the VVRNEI in the XSPEC package. We separately set absorption column densities in the Milky Way ($N_{\text{H,MW}}$) and the LMC ($N_{\text{H,LMC}}$). For the absorption, we used the Tuebingen-Boulder ISM absorption model (TBabs, Wilms et al. 2000) and fixed $N_{\text{H,MW}}$ at 6.0×10^{20} cm $^{-2}$ (Dickey & Lockman 1990). We fixed the initial temperature (kT_{init}) at 0.01 keV, whereas the electron

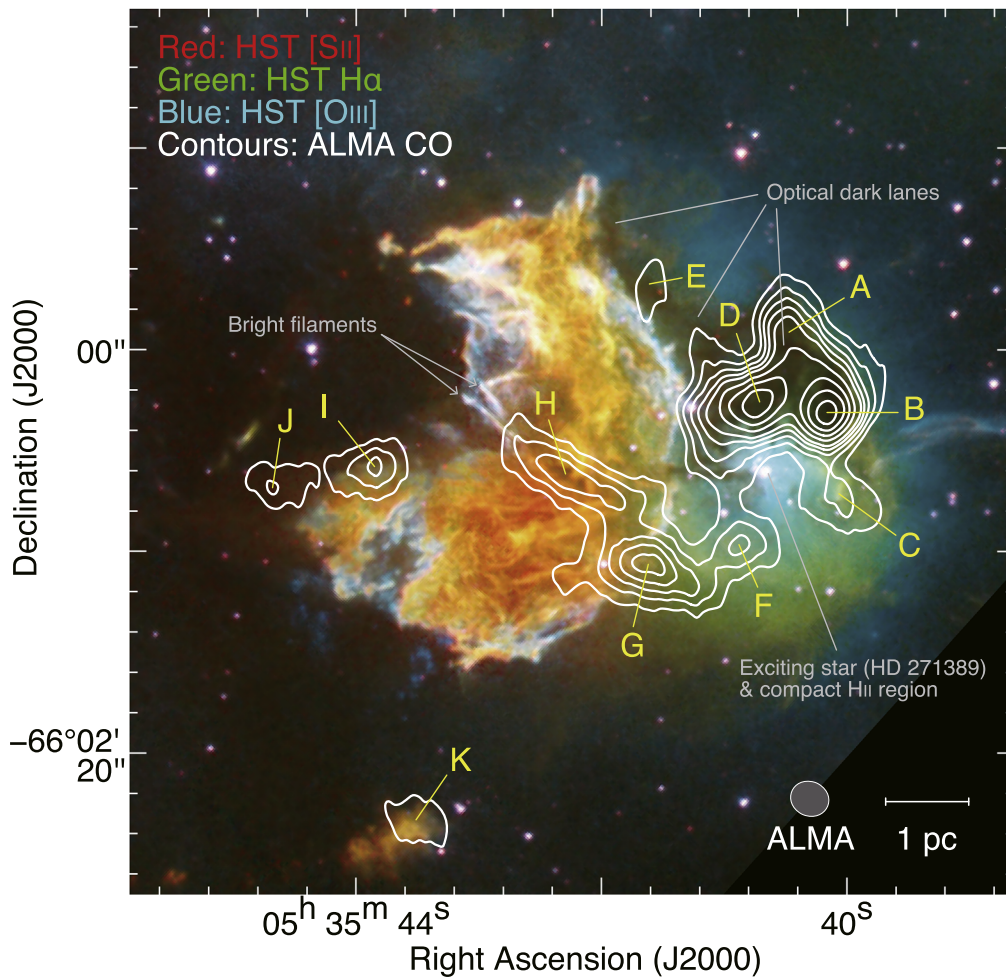


Figure 5. Three-color images of SNR N63A observed by *HST* [Image credit: NASA, ESA, HEIC, and The Hubble Heritage Team (STScI/AURA)]. The red, green, and blue colors represent the [S II], H α , and [O III]. The superposed contours indicate the ALMA CO integrated intensities, whose velocity range is from 277.2 to 284.0 km s $^{-1}$. The contour levels are 6, 12, 18, 24, 30, 40, 50, 60, and 70 K km s $^{-1}$. The CO clouds A–K discussed in Section 3.2 are indicated.

temperature (kT_e), ionization parameter ($n_e t$), and volume emission measure ($VEM = \int n_e n_p dV$) are free parameters. We allowed the abundances to vary for the elements O, Ne, Mg, Si, S, and Fe, whose line emissions can be seen in the X-ray spectrum. The Ar and Ca abundances are linked to S, while Ni is linked to Fe. The other abundances were fixed to the LMC values in the literature (He = 0.89, C = 0.45, N = 0.18, others = 0.50; Russell & Dopita 1992). During the analysis, we used the solar values of Wilms et al. (2000). The NE spectrum above 0.7 keV was reproduced well by this model, but large residuals were left in the 0.5–0.7 keV band ($\chi^2/\text{d.o.f} = 264/143$), as shown in the middle panel of Figure 7(a).

Park et al. (2003, 2012) performed spatial resolved spectral analysis with *Chandra* X-ray data of N49, which is an SNR in the LMC with an age and shock-cloud interaction that is similar to those of N63A. They reproduced the spectra with a two-component NEI model consisting of a higher- kT_e and a lower- kT_e component. Following their approach, we tried the two-component NEI model whose abundances were fixed to the LMC values in the literature (O = 0.21, Ne = 0.28, Mg = 0.33, Si = 0.69, Fe = 0.35; Maggi et al. 2016, He = 0.89, C = 0.45, N = 0.18, others = 0.50; Russell & Dopita 1992). In this fit, $n_e t$ of the lower- kT_e component became larger than 10^{13} cm $^{-3}$ s, indicating that the plasma is in

a collisional ionization equilibrium (CIE) state. Therefore, we fixed $n_e t$ of the component at 10^{13} cm $^{-3}$ s. The residuals above 0.7 keV can be improved by the fit but the other residuals were left in the bands around the line emissions ($\chi^2/\text{d.o.f} = 275/147$; see Figure 7(a)) because the abundance pattern of the higher- kT_e component differs from the LMC values. We therefore allowed the abundances to vary for O, Ne, Mg, Si, S, and Fe for the higher- kT_e component. The NE spectrum is well reproduced ($\chi^2/\text{d.o.f} = 155/141$) by the model consisting of the lower- kT_e CIE and higher- kT_e NEI components with $kT_e = 0.21^{+0.02}_{-0.01}$ keV and $kT_e = 0.70^{+0.02}_{-0.01}$ keV, respectively. The best-fit model and parameters are shown in Figure 7(a) and Table 4, respectively. The best-fit values of the abundances of the higher- kT_e NEI component are far from the LMC values, suggesting that the component originated from the ejecta, whereas the lower- kT_e CIE plasma is a shocked ISM.

We applied the same CIE+NEI model used for NE to the W and SE spectra. The W spectrum can be fitted well (Figure 7(b) and Table 4). On the other hand, the $\chi^2/\text{d.o.f}$ obtained for the SE region was 202/157; hence, a two-component plasma model is rejected because the residuals were left above the 4 keV band (see the middle panels in Figures 7(c) and (d)). We therefore tried two different models; one includes a power-law (PL) component, and the other includes another NEI model.

Table 3
Properties of Molecular Clouds Embedded within the Optical Nebula in SNR N63A

Name	α_{J2000} ($^{\circ} \text{ m s}$)	δ_{J2000} ($^{\circ} \text{ ' ''}$)	T_b (K)	V_{peak} (km s^{-1})	ΔV (km s^{-1})	Size (pc)	Mass (M_{\odot})	$N(\text{H}_2)$ ($\times 10^{22} \text{ cm}^{-2}$)	H_2 Density (cm^{-3})	Ionization State
(1)	(2)	(3)	(4)	(5)	(6)	(7)	(8)	(9)	(10)	(11)
A	5 35 40.52	-66 01 58.8	20.6	280.9	1.4	0.9	170	2.3	7700	photoionized
B	5 35 40.13	-66 02 03.4	28.4	280.9	2.4	1.3	650	5.2	12400	photoionized
C	5 35 40.03	-66 02 06.9	5.4	281.6	1.8	0.8	60	0.9	4900	photoionized
D	5 35 40.73	-66 02 03.0	27.8	280.4	2.1	1.5	730	4.6	7800	photoionized
E	5 35 41.60	-66 01 57.3	9.9	278.3	0.8	0.7	30	0.6	3600	photoionized
F	5 35 40.90	-66 02 10.0	14.5	283.2	1.2	0.9	100	1.3	5400	photoionized
G	5 35 41.60	-66 02 10.8	26.1	282.6	1.1	1.5	360	2.2	4200	shock-ionized
H	5 35 42.39	-66 02 06.1	17.1	282.2	1.3	1.4	270	1.6	4100	shock-ionized
I	5 35 43.87	-66 02 05.9	22.5	280.9	0.8	1.0	110	1.3	4100	shock-ionized
J	5 35 44.70	-66 02 06.8	15.3	280.0	0.9	0.9	80	1.0	3900	shock-ionized
K	5 35 43.42	-66 02 23.3	3.5	282.0	1.7	0.4	10	0.5	6800	shock-ionized

Note. Col. (1): cloud name. Cols. (2)–(7): properties of CO emission obtained by Gaussian fitting. Cols. (2)–(3): position of peak intensity. Col. (4): maximum brightness temperature. Col. (5): center velocity. Col. (6): line width (FWHM). Col. (7): cloud size defined as $2\sqrt{S/\pi}$, where S is the total cloud surface area enclosed by the integrated intensity contour of $\sim 5\sigma$. Col. (8): cloud mass derived using the relation between the molecular hydrogen column density $N(\text{H}_2)$ and $^{12}\text{CO}(J=1-0)$ integrated intensity $W(\text{CO})$ as $N(\text{H}_2) = 7.0 \times 10^{20}[W(\text{CO}) (\text{K km s}^{-1})] (\text{cm}^{-2})$ (Fukui et al. 2008). Col. (9): maximum column density of molecular hydrogen. Col. (10): number density of molecular hydrogen. Col. (11): ionization state of optical nebula associated with the cloud.

We first fitted the SE spectrum with the CIE+NEI+PL model. In this fit, the n_{ct} of the NEI component became larger than $10^{13} \text{ cm}^{-3} \text{ s}$, therefore we fixed it at $10^{13} \text{ cm}^{-3} \text{ s}$. The fit significantly improved the residuals above 4 keV and reproduced the spectrum well ($\chi^2/\text{d.o.f.} = 165/156$). The best-fit model and parameters of the SE region are also shown in Figure 7(c) and Table 4, respectively. In the CIE+2NEI model, kT_e , n_{ct} , and VEM in the additional NEI component were allowed to vary. The abundances became large values (5–300 solar) when these were allowed to vary due to low photon statistics. In fact, fixing abundances at the LMC values, we found that our spectral model fit is equally good. Thus, we take this model fit with abundances fixed at the LMC values as the best-fit model for the CIE+2NEI scenario.

The fit was significantly reduced to $\chi^2/\text{d.o.f.} = 161/154$ and obtained a higher kT_e of $\geq 1.80 \text{ keV}$ and a lower n_{ct} of $1.0_{-0.6}^{+1.4} \times 10^{11} \text{ cm}^{-3} \text{ s}$ than those of the lower- kT_e NEI component (Figure 7(d) and Table 4). The reduced χ^2 in the CIE+2NEI fit is a little smaller than that in the CIE+NEI+PL fit, but this improvement is not statistically significant, with a F-test probability of 0.097. Therefore, we consider two cases in later discussions of the hard X-ray component.

We finally obtained absorbing column densities $N_{\text{H,LMC}}(\text{X-ray})$ of $(1.5\text{--}2.4) \times 10^{21} \text{ cm}^{-2}$ for the NE region, $(4.7\text{--}6.0) \times 10^{21} \text{ cm}^{-2}$ for the SE region, and $(1.9\text{--}2.7) \times 10^{21} \text{ cm}^{-2}$ for the W region.

3.4. Comparison of the ISM and Absorbing Column Density

To estimate the total interstellar proton column density $N_{\text{H}}(\text{H}_2 + \text{H I})$, we use Equation (2) and the following equations (e.g., Dickey & Lockman 1990):

$$N_{\text{H}}(\text{H}_2 + \text{H I}) = 2 \times N(\text{H}_2) + N_{\text{H}}(\text{H I}), \quad (6)$$

$$N_{\text{H}}(\text{H I}) = 1.823 \times 10^{18} W(\text{H I}), \quad (7)$$

where $N_{\text{H}}(\text{H I})$ is the column density of atomic hydrogen and $W(\text{H I})$ is the integrated intensity of H I. In N63A, it is difficult to derive both the $N_{\text{H}}(\text{H I})$ and $W(\text{H I})$ owing to the strong absorption of H I. Then, we assume $W(\text{H I}) = 300\text{--}500 \text{ K km s}^{-1}$ of the SNR from its surroundings. For $N(\text{H}_2)$, we estimate the averaged values

of $W(\text{CO})$ for each region. Then, we obtain $N_{\text{H}}(\text{H I}) \sim (5\text{--}9) \times 10^{20} \text{ cm}^{-2}$ and $2 \times N(\text{H}_2) \sim (0.2\text{--}2.7) \times 10^{22} \text{ cm}^{-2}$, indicating that the atomic hydrogen component is considered negligible in $N_{\text{H}}(\text{H}_2 + \text{H I})$. We finally obtain the total column density of $N_{\text{H}}(\text{H}_2 + \text{H I})$ is $\sim 3 \times 10^{21} \text{ cm}^{-2}$ for the NE region, $\sim 7 \times 10^{21} \text{ cm}^{-2}$ for the SE region, and $\sim 3 \times 10^{22} \text{ cm}^{-2}$ for the W region. These values are $\sim 1.5\text{--}15$ times higher than the absorbing column densities obtained from the X-ray spectra for each region.

4. Discussion

4.1. Dense Molecular Clouds Engulfed by the Shock Waves

N63A is a unique SNR embedded within the large H II region N63, which is also associated with the dense molecular clouds A–K, shock-ionized gas, and photoionized gas. As described in Section 3.2, these dense clouds are certainly associated with both the shock-ionized and photoionized lobes. To be more precise, the eastern molecular clouds G–K are completely embedded within the shock-ionized lobes because the optical dark lane is not clearly seen despite their high density ($\sim 4000\text{--}7000 \text{ cm}^{-3}$, see Table 3). Spatial alignment of shock-ionized filaments with the molecular cloud H is possible evidence for the physical relation among ionized gas, natal dense gas, and shock-survived clouds. In contrast, the western molecular clouds A–F are located just in front of, or partially embedded within, the photoionized lobe because of the presence of an optical dark lane and its pillar-like structures (Figure 5). Both the western and eastern clouds D, E, and J are rim-brightened in soft-band X-rays, suggesting that the surfaces of molecular clouds are selectively ionized by the shock.

Considering the position of the optical nebula—near the center of the SNR—, the shock waves likely propagated from east to west and from the far side to the front side of the molecular clouds, if we assume that the supernova site is near the geometric center of the SNR. This is consistent with the eastern half of the optical nebula being strongly shock-ionized and 70% of GMC mass remaining in the western photoionized lobe. We also confirm that the ionization timescale of

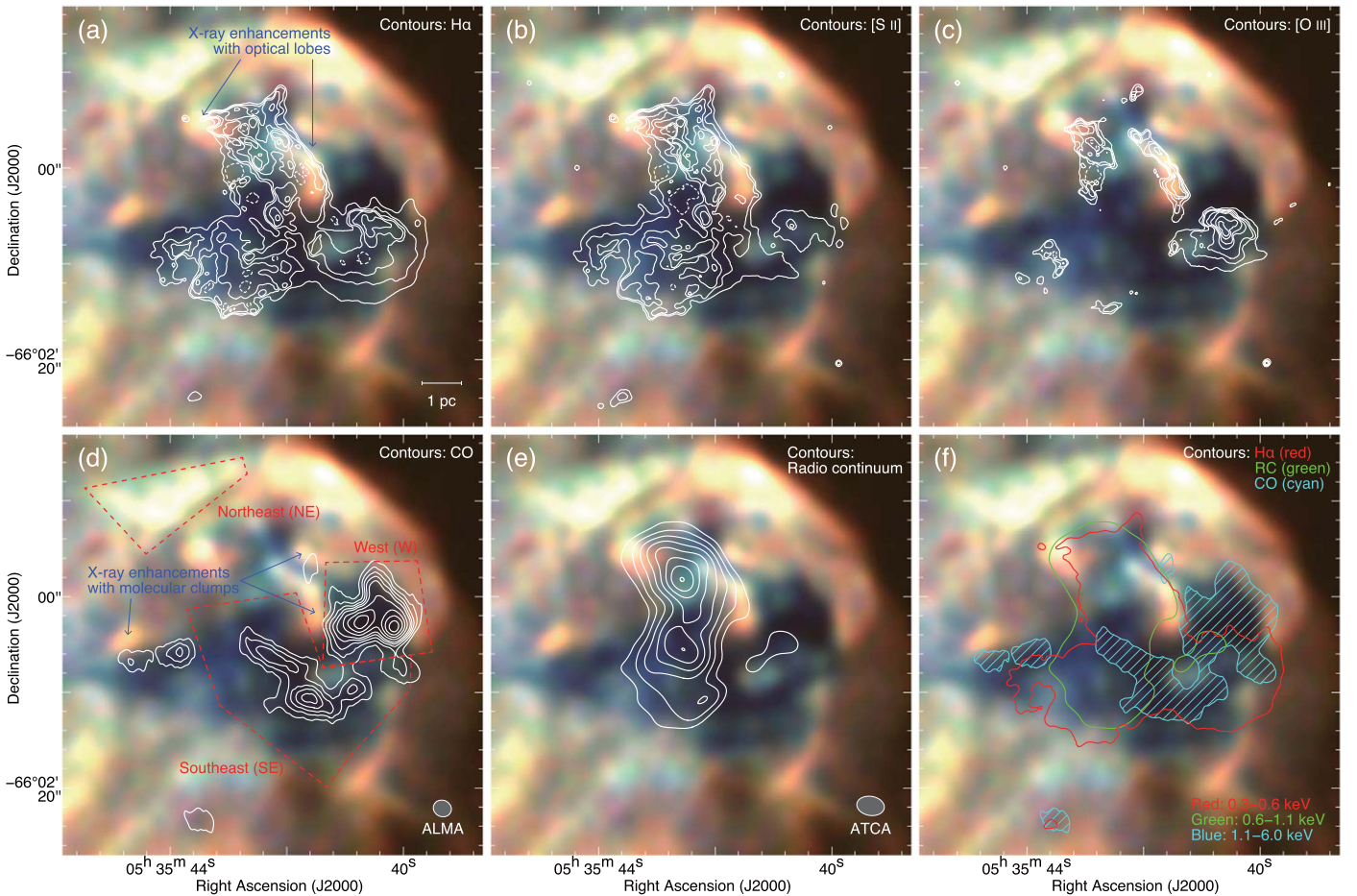


Figure 6. Three-color images of SNR N63A observed by *Chandra*. The red, green, and blue colors represent the energy bands of 0.3–0.6, 0.6–1.1, and 1.1–6.0 keV, respectively. The superposed contours represent (a) H α , (b) [S II], (c) [O III], (d) CO, and (e) the radio continuum with the center frequency of 4786 MHz. The optical contours are smoothed using a median-filter. The integration velocity range and contour levels of CO are the same as in Figure 5. The contour levels are 0.3, 0.5, 0.7, 1.0, 1.5, and 2.0 counts s $^{-1}$ pixel $^{-1}$ for H α ; 0.15, 0.35, 0.7, 1.0, 1.5, and 2.0 counts s $^{-1}$ pixel $^{-1}$ for [S II]; 0.06, 0.08, 0.1, 0.15, 0.2, 0.3, 0.4 for [O III]; 34, 38, 42, 46, 50, 54, 58, and 62 K for radio continuum. We also show boundaries of H α (red), radio continuum (green), and CO (cyan) in (f). Regions of X-ray enhancements are also shown.

shock-ionized lobes is three times longer than that of the photonized lobe using the $n_e t$ values and the ionized gas density (see Table 4 and Section 3.2). Detailed spatially resolved observations using near-infrared lines (e.g., H $_2$, [Fe II], [P II]) and numerical calculations are needed to derive shock parameters.

We also argue that the molecular clouds have been completely engulfed by the shock waves. Because the column densities derived by X-rays ($\sim(1.3\text{--}3.2) \times 10^{21}$ cm $^{-2}$) are significantly smaller than those of the total interstellar protons ($\sim(3\text{--}30) \times 10^{21}$ cm $^{-2}$), the X-ray emitters exist not only behind the molecular clouds, but also in front of the clouds. In addition to this, thermal plasma components with different velocities produced by the forward and reverse shock will possibly be detected. A further X-ray observation with high-spectral-resolution X-ray imaging instruments such as the *X-Ray Imaging and Spectroscopy Mission* will allow us to study the kinematics of thermal plasma components.

Finally, we shall present a possible evolution scenario for N63A and its environments. In the northeastern edge of the LMC, the massive star cluster NGC 2030 was born $\sim 3\text{--}6$ Myr ago (Copetti et al. 1985). There is a small amount of molecular gas owing to the edge of the galaxy (see Yamaguchi et al. 2001), but is still rich in atomic hydrogen (see Kim et al. 2003).

According to Fukui et al. (2017a) and Tsuge et al. (2019), most massive stars in the LMC possibly formed from tidally driven colliding H I flows. Therefore, NGC 2030 also probably formed from H I flows due to the tidal interactions between the LMC and SMC. Subsequently, massive stars including the progenitor of SNR N63A and the exciting star HD 271389 started to evacuate the natal molecular and atomic gas with their strong UV radiation and stellar winds. About 3500 yr ago, the massive progenitor of N63A exploded in the inhomogeneous dense environment. On a large scale, the gas density of the northeast region is much higher than that of the southwest (Figure 2). Therefore, the southwestern X-ray shell shows a diffuse and more expanded morphology, while the northeastern shell mainly collided with the dense H I wall (see Figure 2(c)). Then, the shock waves encountered the western molecular clouds, and now engulf all the molecular clouds associated with the optical nebula.

4.2. Origin of Hard X-Rays

In Section 3.3, we demonstrated that the hard X-ray component of the SW can be described not only with a power-law model, but also with the high-temperature plasma model. In this section, we discuss both cases and their strong relation to the interstellar environment.

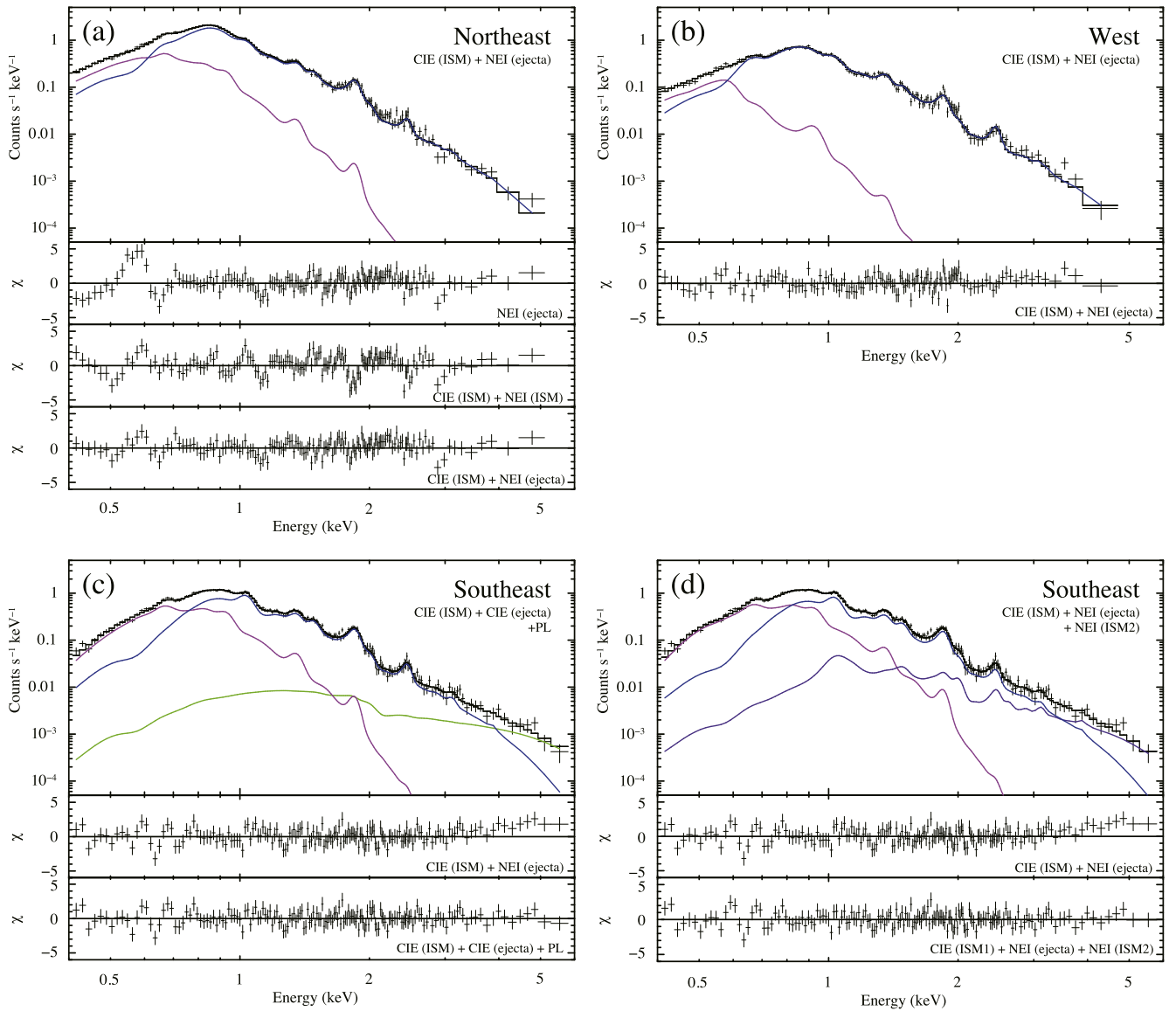


Figure 7. Background-subtracted ACIS-S spectra of the northeast, west, and southeast regions, with the best-fit models shown in the top panels of Figures (a), (b), and (c), (d), respectively. The magenta, blue, green, and purple lines represent the CIE (ISM), NEI/CIE (ejecta), PL, and another NEI (ISM) components, respectively. The black lines show the sum of the components. The bottom and middle panels in each figure indicate the residuals from each model.

4.2.1. Case 1: An Efficient Acceleration of Cosmic-Ray Electrons via the Shock-cloud Interaction

Young SNRs are thought to be primary accelerators of cosmic rays not only in our Galaxy, but also in external galaxies such as the LMC. A supernova shockwave with a velocity of $\sim 3000\text{--}10,000\text{ km s}^{-1}$ provides an ideal site for diffusive shock acceleration (DSA; Bell 1978; Blandford & Ostriker 1978). For the past 20 years, more efficient acceleration mechanisms of cosmic rays have been discussed in both theoretical and observational studies (e.g., reverse shock acceleration: Ellison et al. 2005; nonlinear effects of DSA: Malkov & Drury 2001; magnetic reconnection in the turbulent medium: Hoshino 2012). Shock-cloud interactions also have received attention as an efficient acceleration mechanism of cosmic rays. Fukui et al. (2003) discovered the synchrotron X-ray enhancement toward dense molecular clouds in the northwest of the Galactic young SNR RX J1713.7–3946. Subsequent studies confirmed that many

molecular clouds associated with the SNR are rim-brightened in synchrotron X-rays (Sano et al. 2010, 2013; Sano 2016). Owing to interactions between the shock and inhomogeneous gas distribution—dense gas ($\sim 10^3\text{ cm}^{-3}$) clumps in low-density environments ($\sim 0.01\text{ cm}^{-3}$)—the magnetic field strength is significantly enhanced up to $\sim 1\text{ mG}$ via the strong turbulent motion around the dense gas clumps. Then, we observe bright synchrotron X-rays from the periphery of the molecular clouds. This interpretation is also consistent with MHD simulations (Inoue et al. 2009, 2012). Additionally, similar observational trends are seen in other young SNRs both in the Galaxy and the LMC (e.g., Sano et al. 2015a, 2017b, 2017c; Kuriki et al. 2018; Yamane et al. 2018). X-ray hard spectra are reported toward regions in which the shock-cloud interactions strongly occur, indicating that cosmic rays are efficiently accelerated to higher maximum energies (Sano et al. 2015b; Babazaki et al. 2018).

The young SNR N63A possibly shows observational trends similar to those described above, if the hard X-rays are

Table 4
Best-fit X-Ray Spectral Parameters

Component	Parameter	Northeast	West	Southeast (2 CIE + PL)	Southeast (CIE + 2 NEI)
Absorption	$N_{\text{H,LMC}}$ (10^{21} cm $^{-2}$)	$1.9^{+0.5}_{-0.4}$	$2.1^{+0.6}_{-0.2}$	$5.4^{+0.5}_{-0.6}$	$5.5^{+0.5}_{-0.8}$
	$N_{\text{H,MW}}$ (10^{21} cm $^{-2}$)	0.6 (fixed)	0.6 (fixed)	0.6 (fixed)	0.6 (fixed)
CIE (ISM)	kT_e (keV)	$0.21^{+0.02}_{-0.02}$	$0.12^{+0.04}_{-0.01}$	$0.20^{+0.01}_{-0.01}$	$0.20^{+0.01}_{-0.01}$
	VEM ($\times 10^{59}$ cm $^{-3}$)	$1.8^{+1.0}_{-0.6}$	$1.5^{+1.5}_{-0.8}$	$8.9^{+4.3}_{-3.2}$	$9.9^{+4.4}_{-4.2}$
NEI/CIE (ejecta)	kT_e (keV)	$0.70^{+0.02}_{-0.01}$	$0.73^{+0.01}_{-0.03}$	$0.71^{+0.04}_{-0.03}$	$0.70^{+0.04}_{-0.04}$
	Z_{O} (solar)	$1.72^{+0.35}_{-0.46}$	$3.01^{+3.73}_{-0.97}$	≤ 2.64	≤ 2.54
	Z_{Ne} (solar)	$1.16^{+0.28}_{-0.34}$	$0.89^{+0.75}_{-0.34}$	$3.07^{+3.11}_{-0.73}$	$3.21^{+1.26}_{-0.93}$
	Z_{Mg} (solar)	$0.66^{+0.19}_{-0.14}$	$0.77^{+0.67}_{-0.20}$	$1.22^{+1.35}_{-0.36}$	$1.25^{+0.75}_{-0.46}$
	Z_{Si} (solar)	$0.66^{+0.14}_{-0.13}$	$0.63^{+0.45}_{-0.13}$	$0.89^{+0.95}_{-0.26}$	$0.91^{+0.46}_{-0.26}$
	$Z_{\text{S}} = Z_{\text{Ar}} = Z_{\text{Ca}}$ (solar)	$0.43^{+0.18}_{-0.16}$	$0.87^{+0.67}_{-0.28}$	$0.71^{+0.44}_{-0.24}$	$0.56^{+0.39}_{-0.30}$
	$Z_{\text{Fe}} = Z_{\text{Ni}}$ (solar)	$0.46^{+0.07}_{-0.06}$	$0.42^{+0.37}_{-0.09}$	$0.33^{+0.39}_{-0.11}$	$0.36^{+0.23}_{-0.12}$
	$n_{\text{e}t}$ (10^{11} cm $^{-3}$ s)	≥ 6.5	$4.4^{+4.1}_{-1.4}$	100 (fixed)	≥ 6.1
	VEM ($\times 10^{59}$ cm $^{-3}$)	$1.0^{+0.1}_{-0.1}$	$0.4^{+0.1}_{-0.1}$	$1.1^{+0.3}_{-0.3}$	$1.0^{+0.3}_{-0.4}$
	NEI (ISM2)	kT_e (keV)
$n_{\text{e}t}$ (10^{11} cm $^{-3}$ s)		$1.0^{+1.4}_{-0.6}$
VEM ($\times 10^{57}$ cm $^{-3}$)		$7.1^{+10.6}_{-4.1}$
PL	Γ	$1.7^{+1.5}_{-1.5}$...
	Flux ^a (erg s $^{-1}$ cm $^{-2}$)	1.8×10^{-13}	...
reduced- χ^2 (d.o.f.)		1.10 (141)	1.17 (123)	1.06 (156)	1.04 (154)

Note.

^a The flux is the unabsorbed flux in the 1–10 keV band.

dominated by synchrotron X-rays. Synchrotron X-rays are significantly detected toward the southeast of the optical lobe (Figures 6(d) and 7(b)), corresponding to the shock-ionized region with tiny molecular clouds. This means that the synchrotron X-rays were enhanced via interactions between shocks and dense neutral clumps. To test our interpretation, we compared a hard X-ray image with the CO distribution. Figure 8 shows the RGB image of hard X-rays (E : 4.3–6.0, red), CO (green), and broadband X-rays (E : 0.3–6.0 keV, blue). The energy band of hard X-rays has no line emission and dominantly consists of synchrotron X-rays relative to the thermal component (see Figure 7(b)). We confirm that the hard X-ray bright spot, peak A, spatially corresponds to the shock-ionized region with clumpy neutral gas. We also note that the molecular cloud K is also associated with one of the minor peaks of hard X-rays, indicating that the shock-cloud interaction also occurred. However, there is no dense molecular cloud toward peak B and the other two minor peaks of hard X-rays. We hypothesize that these hard X-ray peaks are possibly associated with a cold HI clump with a density of a few 100 cm $^{-3}$. In fact, Warren et al. (2003) mentioned the presence of interstellar absorption toward hard X-ray peak B. Moreover, it is known that the cold HI clumps also enhance the synchrotron X-ray enhancement (e.g., RX J1713.7–3946, Sano et al. 2013; RCW 86, Sano et al. 2017c). To confirm this scenario, detailed HI observations and X-ray imaging spectroscopy are needed.

4.2.2. Case 2: High-temperature Plasma toward the Shocked Molecular Clouds

Here we discuss the alternative idea that the hard X-rays originated from the high-temperature plasma of shocked ISM. In the SE region of N63A, the supernova shock may strongly interact with clumpy and dense molecular clouds, developing

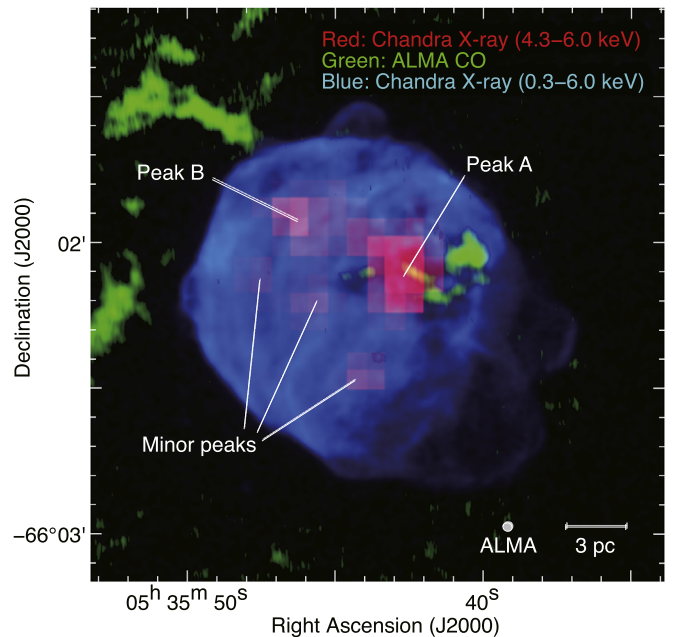


Figure 8. Same three-color image as in Figure 3, but the red color represents *Chandra* X-rays in the energy band of 4.3–6.0 keV.

multiple reflected shock structures to heat the gas up to high temperatures. In this scenario, the reheated gas may be either underabundant ISM or overabundant ejecta. Unfortunately, we could not distinguish them through X-ray spectroscopy alone due to the low photon statistics. However, the morphological structure of hard X-rays (Figure 8) favors a shocked ISM origin. We note that the spatial extent of the hard-X-rays toward peak A is very similar to that of the shock-ionized optical lobe (see also in Figures 4 and 5), indicating that the

hard X-rays possibly have the same origin as the shock-ionized optical lobe.

The $n_e t$ value also supports recent heating of dense molecular clouds. Assuming the depth of the emitting region to be 3 pc, the spatial extent of the shock-ionized optical lobe, the emission volume of SE is estimated to be $V = 1.3 \times 10^{57} \text{ cm}^3$. Therefore, the VEM of high-temperature plasma in the SE region corresponds to the electron density of $n_e = 2.5 f^{-0.5} \text{ cm}^{-3}$, where f is the filling factor for this component. We then derive the elapsed time since the dense molecular clouds was heated, $t = 4.0 \times 10^{10} f^{0.5} \text{ s} < 1300 \text{ yr}$. This value is much lower than the maximum age of 5000 yr, hence the high-temperature plasma likely has been heated recently. This situation is very similar to those of Magellanic SNR N49 and Galactic SNR RCW 86 (Park et al. 2003; Yamaguchi et al. 2008). To confirm this scenario, we need more detailed studies of spatially resolved X-ray spectroscopy for the whole remnant.

4.3. Ionized Gas as a Target of Cosmic-Ray Protons

Interstellar gas associated with SNRs also plays an important role in understanding the origin of gamma-rays. The gamma-rays from young SNRs are thought to be produced by two mechanisms: the hadronic process and the leptonic process. The former is due to the decay of neutral pions produced by interactions between accelerated cosmic-ray protons and interstellar protons, while the latter occurs when a cosmic-ray electron energizes a low-energy photon to gamma-ray energies via the inverse Compton effect. The non-thermal bremsstrahlung of cosmic-ray electrons is also one of the origins of leptonic gamma-rays. For the young SNRs, however, the non-thermal bremsstrahlung is negligible (e.g., H.E.S.S. Collaboration et al. 2018a, 2018b, 2018c).

If the hadronic process is dominant, a good spatial correlation between the interstellar protons and gamma-rays is expected. Fukui et al. (2012) demonstrated such spatial correspondence in the young SNR RX J1713.7–3946 for the first time. The authors took into account both the molecular and atomic components as the interstellar protons, and then derived an averaged interstellar proton density of $\sim 130 \text{ cm}^{-3}$. The total energy of cosmic-ray protons is also estimated to be $\sim 10^{48}$ erg, corresponding to $\sim 0.1\%$ of the typical kinematic energy of a supernova explosion. Subsequent studies of both the young and middle-aged SNRs showed similar values for the total cosmic-ray energy, $\sim 10^{48}$ – 10^{49} erg (e.g., Yoshiike et al. 2013, 2017; Fukuda et al. 2014; Fukui et al. 2017b; Kuriki et al. 2018; Sano et al. 2018b).

Most recently, Campana et al. (2018) presented a significant detection of GeV gamma-rays from SNR N63A, which was confirmed with 9 year *Fermi* Large-Area Telescope data. Owing to the coarse angular resolution, we could not compare the gamma-ray image with the gas distribution. The gamma-ray flux (E : 1–10 GeV) was estimated to be $(6\text{--}12) \times 10^{-7} \text{ MeV cm}^{-2} \text{ s}^{-1}$, corresponding to the gamma-ray luminosity $L_\gamma(1\text{--}10 \text{ GeV})$ of $\sim (1.3\text{--}5.8) \times 10^{35} (d/50 \text{ kpc})^2 \text{ erg s}^{-1}$, where d is the distance of the source. If the gamma-ray spectrum is dominated by a hadronic origin, the total energy of cosmic-ray protons W_p is given by the following equation (e.g., Aharonian et al. 2006):

$$W_p \sim t_{pp \rightarrow \pi_0} \times L_\gamma, \quad (8)$$

where $t_{pp \rightarrow \pi_0} \sim 4.5 \times 10^{15} (n/1 \text{ cm}^{-3})^{-1} \text{ s}$ is the characteristic cooling time of protons, and n is the number density of interstellar protons. We then finally obtain the total energy of cosmic-ray protons $W_p(1\text{--}10 \text{ GeV})$ as follows:

$$W_p \sim 0.6\text{--}2.6 \times 10^{51} (n/1 \text{ cm}^{-3})^{-1} (d/50 \text{ kpc})^2 \text{ erg}. \quad (9)$$

In general, n is derived as “neutral gas density,” consisting of both the molecular and atomic components (e.g., Fukui et al. 2012), because the shock-ionization effect is negligible even for the middle-aged SNRs W44 and IC443 (e.g., Yoshiike et al. 2013, 2017). For the case of N63A, however, most neutral molecular clouds have been ionized, especially toward the eastern half of the optical nebula. In addition to this, the low-energy cosmic-ray protons traced by the *Fermi* data cannot penetrate into the dense molecular clouds. According to Inoue et al. (2012), the penetration depth l_{pd} of cosmic-ray protons is

$$l_{pd} \sim 0.002 \eta^{0.5} (E/1 \text{ GeV})^{0.5} (B/100 \mu\text{G})^{-0.5} \times (t_{\text{age}}/3500 \text{ yr})^{0.5} (\text{pc}), \quad (10)$$

where $\eta = B^2/\delta B^2 \gtrsim 1$ is a turbulence factor defined as the degree of magnetic field fluctuations, E is the energy of cosmic-ray protons, B is the magnetic field strength, and t_{age} is the age of the SNR. The magnetic field strength B in the Galactic molecular clouds is given by the following equation (Crutcher et al. 2010):

$$B \sim 10 (n/300 \text{ cm}^{-3})^{0.65} (\mu\text{G}), \quad (11)$$

where n is the number density of protons in molecular clouds. In SNR N63A, we estimate the magnetic field strength $B \sim 80\text{--}180 \mu\text{G}$ in the molecular clouds associated with N63A (see Table 3), assuming the Equation (11) to hold for the LMC. The GeV gamma-ray flux of N63A is measured from 1 to 10 GeV, corresponding to the cosmic-ray proton energy of 10–100 GeV if the hadronic process dominates. The penetration depth l_{pd} is therefore to be 0.005–0.03 pc if we assume $\eta = 1$ under the shock-cloud interaction (e.g., Uchiyama et al. 2007). The penetration depth is significantly smaller than the size of the molecular clouds (see Table 3), indicating that the molecular cloud in N63A may not be a target of the low-energy cosmic-ray protons. We therefore use the total ISM proton density consisting of both ionized gas and neutral atomic hydrogen. Using Equations (5), we derive the averaged ionized gas density to be $\sim 110 \pm 70 \text{ cm}^{-3}$ assuming $L_1 \sim 15 \text{ pc}$ (\sim diameter of the radio bright shell) and $T_e \sim 14743 \text{ K}$ for the whole SNR. In Section 3.4, we derived the atomic hydrogen column density as $(5\text{--}9) \times 10^{20} \text{ cm}^{-2}$ using the HI data. We divided it by twice the shell thickness of $\sim 3 \text{ pc}$, which is estimated by a three-dimensional Gaussian fitting of the northeastern X-ray shell (see Sano et al. 2017b). We finally obtain a neutral atomic hydrogen density of $\sim 80 \pm 20 \text{ cm}^{-3}$ and a total ISM proton density of $\sim 190 \pm 90 \text{ cm}^{-3}$. The total energy of cosmic-ray protons is then estimated to be $\sim (0.3\text{--}1.4) \times 10^{49} \text{ erg}$, corresponding to $\sim 0.3\%\text{--}1.4\%$ of the typical kinematic energy released by a single supernova. These values are roughly consistent with the Galactic SNRs (e.g., Sano et al. (2018b) and references therein). Further gamma-ray

observations using the Cherenkov Telescope Array (CTA) will allow us to study the gamma-ray morphology and spectrum of N63A in detail.

5. Conclusions


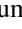
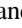





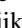
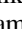
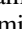
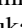

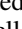
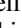
In the present study, we have carried out new $^{12}\text{CO}(J = 1-0, 3-2)$ observations of LMC SNR N63A using ASTE and ALMA with angular resolutions of $\sim 0.4-6$ pc. Our primary conclusions are summarized as follows.

1. We have found three GMCs toward the northeast, east, and near the center of SNR N63A using ASTE $^{12}\text{CO}(J = 3-2)$ data. The cloud size is $\sim 7-10$ pc and the total mass of the GMCs is $\sim 1 \times 10^4 M_{\odot}$. Using ALMA $^{12}\text{CO}(J = 1-0)$ data, we spatially resolved the GMC into 11 molecular clouds, which are embedded within the optical nebula. The total masses of the molecular clouds are $\sim 800 M_{\odot}$ for the shock-ionized region and $\sim 1700 M_{\odot}$ for the photoionized region. The densest molecular clouds A, B, and D show a good spatial correspondence with the optical dark lane, indicating that most of these clouds are located in front of the photoionized nebula. On the other hand, molecular clouds G–K are placed inside or behind the shock-ionized lobes. The extent of the X-ray hole coincides with that of the CO clouds, $\text{H}\alpha$ nebula, and radio continuum, indicating that the interstellar absorption of X-rays is caused not only by the dense molecular clouds, but also by the ionized gas cloud.
2. A spatially resolved X-ray spectroscopy has revealed that the absorbing column densities toward the molecular clouds are $\sim (1.5-6.0) \times 10^{21} \text{ cm}^{-2}$, which are $\sim 1.5-15$ times less than the averaged interstellar proton column densities. This indicates that all the dense molecular clouds have been completely engulfed by the shock waves, but still survive from erosion owing to their high density and short interacting time. The X-ray spectrum toward the shocked molecular clumps is also well fitted by the models consisting not only of absorbed CIE, NEI, and power-law components, but also with absorbed CIE and two NEI components. The former indicates that the shock-cloud interaction possibly enhances the synchrotron X-ray flux and/or the maximum energy of cosmic-ray electrons through amplifications of the magnetic field strength and turbulence motion. For the latter case, shock-cloud interactions developed multiple reflected shock structures to heat the gas up to high temperature roughly 1300 yr ago or less.
3. For SNR N63A, the ionized gas may act as a target of the accelerated cosmic-ray protons because most natal molecular clouds have been ionized by the shock. If the GeV gamma-rays from N63A are dominated by a hadronic origin, the total energy of cosmic-ray protons is calculated to be $\sim (0.3-1.4) \times 10^{49}$ erg with an estimated ISM proton density of $\sim 190 \pm 90 \text{ cm}^{-3}$, containing both the shock-ionized gas and neutral atomic hydrogen. This value corresponds to $\sim 0.3\%-1.4\%$ of the typical kinematic energy of a single supernova, roughly consistent with the Galactic SNRs. Further gamma-ray observations using the CTA will allow us to study the gamma-ray morphology and spectrum of N63A in detail.

This paper makes use of the following ALMA data: ADS/JAO.ALMA #2015.1.01130.S. ALMA is a partnership of ESO (representing its member states), NSF (USA) and NINS (Japan), together with NRC (Canada), NSC and ASIAA (Taiwan), and KASI (Republic of Korea), in cooperation with the Republic of Chile. The Joint ALMA Observatory is operated by ESO, AUI/NRAO, and NAOJ. The scientific results reported in this article are based on data obtained from the *Chandra* Data Archive (Obs ID: 777). This research has made use of software provided by the Chandra X-ray Center (CXC) in the application packages CIAO (v 4.10). This study was financially supported by Grants-in-Aid for Scientific Research (KAKENHI) of the Japanese Society for the Promotion of Science (JSPS; grants No. 15H05694, 16K17664, and 18J01417). H.S. is supported by “Building of Consortia for the Development of Human Resources in Science and Technology” of the Ministry of Education, Culture, Sports, Science and Technology (MEXT; grant No. 01-M1-0305). H.M. is supported by the World Premier International Research Center Initiative (WPI). K. Tokuda is supported by NAOJ ALMA Scientific Research (grant No. 2016-03B). M.S. acknowledges support by the Deutsche Forschungsgemeinschaft (DFG) through the Heisenberg professor grant SA 2131/5-1 and the research grant SA 2131/4-1. We really appreciate the anonymous referee for the useful comments and suggestions, which helped us to improve the paper.

Software: CASA (v5.1.0.: McMullin et al. 2007), CIAO (v 4.10: Fruscione et al. 2006), MIRIAD (Sault et al. 1995), KARMA (Gooch 1997).

ORCID iDs

H. Sano  <https://orcid.org/0000-0003-2062-5692>
H. Matsumura  <https://orcid.org/0000-0001-6533-224X>
Y. Yamane  <https://orcid.org/0000-0001-8296-7482>
R. Z. E. Alsaberi  <https://orcid.org/0000-0001-5609-7372>
M. D. Filipović  <https://orcid.org/0000-0002-4990-9288>
K. Tachihara  <https://orcid.org/0000-0002-1411-5410>
K. Tokuda  <https://orcid.org/0000-0002-2062-1600>
K. Tsuge  <https://orcid.org/0000-0002-2794-4840>
S. Yoshiike  <https://orcid.org/0000-0002-2458-7876>
A. Kawamura  <https://orcid.org/0000-0001-7813-0380>
T. Minamidani  <https://orcid.org/0000-0001-9778-6692>
S. Inutsuka  <https://orcid.org/0000-0003-4366-6518>
N. Maxted  <https://orcid.org/0000-0003-2762-8378>
G. Rowell  <https://orcid.org/0000-0002-9516-1581>
M. Sasaki  <https://orcid.org/0000-0001-5302-1866>

References

- Aharonian, F., Akhperjanian, A. G., Bazer-Bachi, A. R., et al. 2006, *A&A*, **449**, 223
Allen, M. G., Groves, B. A., Dopita, M. A., Sutherland, R. S., & Kewley, L. J. 2008, *ApJS*, **178**, 20
Babazaki, Y., Mitsuishi, I., Matsumoto, H., et al. 2018, *ApJ*, **864**, 12
Bell, A. R. 1978, *MNRAS*, **182**, 147
Blandford, R. D., & Ostriker, J. P. 1978, *ApJL*, **221**, L29
Bojičić, I. S., Filipović, M. D., Parker, Q. A., et al. 2007, *MNRAS*, **378**, 1237
Bozzetto, L. M., & Filipović, M. D. 2014, *Ap&SS*, **351**, 207
Bozzetto, L. M., Filipović, M. D., Crawford, E. J., et al. 2010, *SerAJ*, **181**, 43
Bozzetto, L. M., Filipović, M. D., Crawford, E. J., et al. 2012a, *MNRAS*, **420**, 2588
Bozzetto, L. M., Filipović, M. D., Crawford, E. J., et al. 2012b, *RMxAA*, **48**, 41
Bozzetto, L. M., Filipović, M. D., Crawford, E. J., et al. 2013, *MNRAS*, **432**, 2177

- Bozzetto, L. M., Filipovic, M. D., Crawford, E. J., De Horta, A. Y., & Stupar, M. 2012c, *SerAJ*, **184**, 69
- Bozzetto, L. M., Filipovic, M. D., Urosevic, D., & Crawford, E. J. 2012d, *SerAJ*, **185**, 25
- Bozzetto, L. M., Filipović, M. D., Urošević, D., Kothes, R., & Crawford, E. J. 2014b, *MNRAS*, **440**, 3220
- Bozzetto, L. M., Filipović, M. D., Vukotić, B., et al. 2017, *ApJS*, **230**, 2
- Bozzetto, L. M., Kavanagh, P. J., Maggi, P., et al. 2014a, *MNRAS*, **439**, 1110
- Brantseg, T., McEntaffer, R. L., Bozzetto, L. M., Filipovic, M., & Grieves, N. 2014, *ApJ*, **780**, 50
- Cajko, K. O., Crawford, E. J., & Filipovic, M. D. 2009, *SerAJ*, **179**, 55
- Campana, R., Massaro, E., & Bernieri, E. 2018, *Ap&SS*, **363**, 144
- Cault, A., & Williams, R. M. 2012, *ApJ*, **761**, 107
- Celli, S., Morlino, G., Gabici, S., & Aharonian, F. 2018, arXiv:1804.10579
- Chu, Y.-H. 2001, in AIP Conf. Proc. 565, Young Supernova Remnants, ed. S. S. Holt & U. Hwang (Melville: AIP), 409
- Chu, Y.-H., & Kennicutt, R. C., Jr. 1988, *AJ*, **96**, 1874
- Cohen, R. S., Dame, T. M., Garay, G., et al. 1988, *ApJL*, **331**, L95
- Copetti, M. V. F., Pastoriza, M. G., & Dottori, H. A. 1985, *A&A*, **152**, 427
- Cornwell, T. J. 2008, ISTSP, 565, 409
- Cox, D. P., & Raymond, J. C. 1985, *ApJ*, **298**, 651
- Crawford, E. J., Filipovic, M. D., de Horta, A. Y., Stootman, F. H., & Payne, J. L. 2008a, *SerAJ*, **177**, 61
- Crawford, E. J., Filipović, M. D., Haberl, F., et al. 2010, *A&A*, **518**, A35
- Crawford, E. J., Filipovic, M. D., & Payne, J. L. 2008b, *SerAJ*, **176**, 59
- Crutcher, R. M., Wandelt, B., Heiles, C., Falgarone, E., & Troland, T. H. 2010, *ApJ*, **725**, 466
- Desai, K. M., Chu, Y.-H., Gruendl, R. A., et al. 2010, *AJ*, **140**, 584
- Dickel, J. R., Milne, D. K., Junkes, N., & Klein, U. 1993, *A&A*, **275**, 265
- Dickey, J. M., & Lockman, F. J. 1990, *ARA&A*, **28**, 215
- Ellison, D. C., Decourchelle, A., & Ballet, J. 2005, *A&A*, **429**, 569
- Ezawa, H., Kawabe, R., Kohno, K., & Yamamoto, S. 2004, *Proc. SPIE*, **5489**, 763
- Fruscione, A., McDowell, J. C., Allen, G. E., et al. 2006, *Proc. SPIE*, **6270**, 62701V
- Fukuda, T., Yoshiike, S., Sano, H., et al. 2014, *ApJ*, **788**, 94
- Fukui, Y., Kawamura, A., Minamidani, T., et al. 2008, *ApJS*, **178**, 56
- Fukui, Y., Mizuno, N., Yamaguchi, R., et al. 1999, *PASJ*, **51**, 745
- Fukui, Y., Moriguchi, Y., Tamura, K., et al. 2003, *PASJ*, **55**, L61
- Fukui, Y., Sano, H., Sato, J., et al. 2012, *ApJ*, **746**, 82
- Fukui, Y., Sano, H., Sato, J., et al. 2017b, *ApJ*, **850**, 71
- Fukui, Y., Tsuge, K., Sano, H., et al. 2017a, *PASJ*, **69**, L5
- Gooch, R. E. 1997, *PASA*, **14**, 106
- Haberl, F., Filipović, M. D., Bozzetto, L. M., et al. 2012, *A&A*, **543**, A154
- H.E.S.S. Collaboration, Abdalla, H., Abramowski, A., et al. 2018a, *A&A*, **612**, A6
- H.E.S.S. Collaboration, Abdalla, H., Abramowski, A., et al. 2018b, *A&A*, **612**, A7
- H.E.S.S. Collaboration, Abramowski, A., Aharonian, F., et al. 2018c, *A&A*, **612**, A4
- Hoshino, M. 2012, *PhRvL*, **108**, 135003
- Hughes, J. P., Hayashi, I., & Koyama, K. 1998, *ApJ*, **505**, 732
- Inoue, T., Yamazaki, R., & Inutsuka, S.-i. 2009, *ApJ*, **695**, 825
- Inoue, T., Yamazaki, R., Inutsuka, S.-i., & Fukui, Y. 2012, *ApJ*, **744**, 71
- Israel, F. P., Johansson, L. E. B., Lequeux, J., et al. 1993, *A&A*, **276**, 25
- Jenkins, E. B., & Savage, B. D. 1974, *ApJ*, **187**, 243
- Kavanagh, P. J., Sasaki, M., Bozzetto, L. M., et al. 2015, *A&A*, **583**, A121
- Kawamura, A., Mizuno, Y., Minamidani, T., et al. 2009, *ApJS*, **184**, 1
- Kim, S., Dopita, M. A., Staveley-Smith, L., & Bessell, M. S. 1999, *AJ*, **118**, 2797
- Kim, S., Staveley-Smith, L., Dopita, M. A., et al. 2003, *ApJS*, **148**, 473
- Kuriki, M., Sano, H., Kuno, N., et al. 2018, *ApJ*, **864**, 161
- Laval, A., Greve, A., & van Genderen, A. M. 1986, *A&A*, **164**, 26
- Levenson, N. A., Kirshner, R. P., Blair, W. P., & Winkler, P. F. 1995, *AJ*, **110**, 739
- Lucke, P. B., & Hodge, P. W. 1970, *AJ*, **75**, 171
- Maggi, P., Haberl, F., Kavanagh, P. J., et al. 2016, *A&A*, **585**, A162
- Malkov, M. A., & Drury, L. O. 2001, *RPPH*, **64**, 429
- Mathewson, D. S., Ford, V. L., Dopita, M. A., et al. 1983, *ApJS*, **51**, 345
- McKee, C. F., & Ostriker, J. P. 1977, *ApJ*, **218**, 148
- McMullin, J. P., Waters, B., Schiebel, D., Young, W., & Golap, K. 2007, adass XVI, 376, 127
- Minamidani, T., Tanaka, T., Mizuno, Y., et al. 2011, *AJ*, **141**, 73
- Oey, M. S. 1996, *ApJS*, **104**, 71
- Park, S., Burrows, D. N., Garmire, G. P., et al. 2003, *ApJ*, **586**, 210
- Park, S., Hughes, J. P., Slane, P. O., et al. 2012, *ApJ*, **748**, 117
- Payne, J. L., White, G. L., & Filipović, M. D. 2008, *MNRAS*, **383**, 1175
- Pecaut, M. J., & Mamajek, E. E. 2013, *ApJS*, **208**, 9
- Russell, S. C., & Dopita, M. A. 1992, *ApJ*, **384**, 508
- Sano, H. 2016, Shock–Cloud Interaction in RX J1713.7–3946: Evidence for Cosmic-ray Acceleration in the Young VHE γ -ray Supernova Remnant (1st ed.; Tokyo: Springer Japan)
- Sano, H., Fujii, K., Yamane, Y., et al. 2017a, in AIP Conf. Proc. 1792, 6th International Meeting on High Energy Gamma-Ray Astronomy, ed. F. A. Aharonian, W. Hofmann, & M. Frank (Melville, NY: AIP), 040038
- Sano, H., Fukuda, T., Yoshiike, S., et al. 2015b, *ApJ*, **799**, 175
- Sano, H., Fukui, Y., Yoshiike, S., et al. 2015a, in ASP Conf. Ser. 499, Revolution in Astronomy with ALMA: The Third Year 499, ed. D. Iono et al. (San Francisco, CA: ASP), 257
- Sano, H., Reynoso, E. M., Mitsuishi, I., et al. 2017c, *JHEAp*, **15**, 1
- Sano, H., Rowell, G., Reynoso, E. M., et al. 2018b, arXiv:1805.10647
- Sano, H., Sato, J., Horachi, H., et al. 2010, *ApJ*, **724**, 59
- Sano, H., Tanaka, T., Torii, K., et al. 2013, *ApJ*, **778**, 59
- Sano, H., Yamane, Y., Tokuda, K., et al. 2018a, *ApJ*, **867**, 7
- Sano, H., Yamane, Y., Voisin, F., et al. 2017b, *ApJ*, **843**, 61
- Sault, R. J., Teuben, P. J., & Wright, M. C. H. 1995, adass IV, **77**, 433
- Sault, R. J., & Wieringa, M. H. 1994, *A&AS*, **108**, 585
- Shull, P., Jr. 1983, *ApJ*, **275**, 592
- Sorai, K., Sunada, K., Okumura, S. K., et al. 2000, *Proc. SPIE*, **4015**, 86
- Tsuge, K., Sano, H., Tachihara, K., et al. 2019, *ApJ*, **871**, 44
- Uchiyama, Y., Aharonian, F. A., Tanaka, T., Takahashi, T., & Maeda, Y. 2007, *Natur*, **449**, 576
- van den Bergh, S., & Dufour, R. J. 1980, *PASP*, **92**, 32
- Warren, J. S., Hughes, J. P., & Slane, P. O. 2003, *ApJ*, **583**, 260
- Williams, R. M., Chu, Y.-H., & Gruendl, R. 2006, *AJ*, **132**, 1877
- Wilms, J., Allen, A., & McCray, R. 2000, *ApJ*, **542**, 914
- Yamaguchi, H., Badenes, C., Petre, R., et al. 2014, *ApJL*, **785**, L27
- Yamaguchi, H., Koyama, K., Nakajima, H., et al. 2008, *PASJ*, **60**, S123
- Yamaguchi, R., Mizuno, N., Onishi, T., Mizuno, A., & Fukui, Y. 2001, *ApJL*, **553**, L185
- Yamane, Y., Sano, H., van Loon, J. T., et al. 2018, *ApJ*, **863**, 55
- Yoshiike, S., Fukuda, T., Sano, H., et al. 2013, *ApJ*, **768**, 179
- Yoshiike, S., Fukuda, T., Sano, H., & Fukui, Y. 2017, in AIP Conf. Proc. 1792, 6th International Meeting on High Energy Gamma-Ray Astronomy, ed. F. A. Aharonian, W. Hofmann, & M. Frank (Melville, NY: AIP), 040039